



Sub-mesoscale ocean vortex trains in the Luzon Strait

Quanan Zheng,^{1,2} Hui Lin,² Junmin Meng,^{2,3} Xiaomin Hu,³ Y. Tony Song,⁴ Yuanzhi Zhang,² and Chunyan Li⁵

Received 30 May 2007; revised 21 August 2007; accepted 25 January 2008; published 25 April 2008.

[1] This study uses the Argos satellite-tracked surface drifter trajectory data and ENVISAT (European satellite) ASAR (advanced synthetic aperture radar) images to illustrate the ocean vortex trains (OVT) in the Luzon Strait. Two cases that occurred in the northwest of Babuyan Island are observed. The first train of three cyclonic vortices showed up on drifter trajectories from 20° to 20.5°N and from 120° to 121°E, and the second, consisting of five pairs of cyclonic-anticyclonic vortices, occurred on the upstream side of the first one from 19.5° to 20.0°N and from 121.0° to 122.0°E and showed up on the ASAR images acquired on 19 November 2006. The total length of the vortex train axis reaches about 250 km. All vortices propagate northwestward ($\sim 315^\circ$ TN). The mean angular velocity is $(2.07 \pm 0.18) \times 10^{-5} \text{ s}^{-1}$. Theoretical models of ocean vortex radar image derived from radar imaging theories are used to extract dynamical parameters from ASAR imagery signatures, which include the distance between two consecutive vortices and that between two rows of vortices of $(22.6 \pm 1.9) \text{ km}$ and $(8.2 \pm 1.2) \text{ km}$, respectively, the maximum rotational velocity radius as 4.70 km, and the vortex rotational angular velocity $3 \times 10^{-5} \text{ s}^{-1}$. Dynamical analyses give the mean velocity of the current of 0.65 ms^{-1} , and the propagation velocity of the vortex 0.58 ms^{-1} . The vortex shedding rate is estimated as $2.57 \times 10^{-5} \text{ s}^{-1}$. The Reynolds number is estimated as 50 to 500. For the individual vortex and the vortex train, the Rossby numbers are $O(0.4)$, and $O(0.5)$, respectively, implying that both vortex and vortex train observed in the Luzon Strait have a sub-mesoscale nature. This study also reveals a strong current with an average surface current velocity of around 0.7 ms^{-1} and the direction of around 315° TN flowing directly from the Pacific to SCS passing through the southern Luzon Strait. The mean flow velocity can be calculated using methods developed in this study and OVT dynamical models. This information may provide more insight to the circulation systems in the area including the origin of Kuroshio.

Citation: Zheng, Q., H. Lin, J. Meng, X. Hu, Y. T. Song, Y. Zhang, and C. Li (2008), Sub-mesoscale ocean vortex trains in the Luzon Strait, *J. Geophys. Res.*, 113, C04032, doi:10.1029/2007JC004362.

1. Introduction

[2] The vortex train is a phenomenon well documented in classical text books of fluid dynamics [e.g., Kundu, 1990]. Field observations and laboratory simulations indicate that when an object is placed in a steadily flowing fluid, the object will form a source of disturbance to the fluid flow. The downstream flow behind this obstacle will become

unstable. Once the flow speed U and the body width D satisfy a certain relation (Reynolds number $UD/\nu \gg 10$, in which ν is the viscosity of fluid), two parallel rows of alternating vortices with opposite rotations will be generated. This kind of vortex train is commonly called a Kármán vortex street (KVS) [Von Kármán, 1954; Chopra and Hubert, 1964; Taneda, 1965; Kundu, 1990].

[3] In recent years, the KVS in the lower atmosphere occurring on the lee side of the separate mountain peaks or islands has been studied using the satellite images. On visible band images, the atmospheric KVS shows up through modulated cloud patterns [Tsuchiya, 1969; Thomson *et al.*, 1977; Turner and Warren, 1988]. While on synthetic aperture radar (SAR) images, the atmospheric KVS shows up through modulation to the spatial distribution of ocean surface small waves [Li *et al.*, 2000]. These satellite images can provide a two-dimensional, plane-view of KVS. By interpreting the satellite images, the fine structures and dynamic parameters of KVS can be obtained [Li *et al.*, 2000].

¹Department of Atmospheric and Oceanic Science, University of Maryland, College Park, Maryland, USA.

²Institute of Space and Earth Information Sciences, The Chinese University of Hong Kong, Shatin, Hong Kong.

³The Key Laboratory of Marine Science and Numerical Modeling, The First Institute of Oceanography, State Oceanic Administration, Qingdao, China.

⁴Jet Propulsion Laboratory, California Institute of Technology, Pasadena, California, USA.

⁵Coastal Studies Institute, Department of Oceanography and Coastal Sciences, Louisiana State University, Baton Rouge, Louisiana, USA.

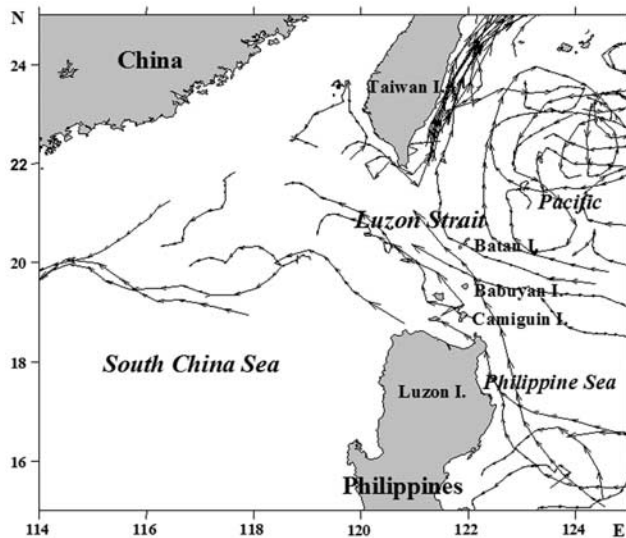


Figure 1. A map of study area. Lines with arrows are Argos satellite-tracked surface drifter trajectories in November. The trajectories show a train of three cyclonic vortices northwest of Babuyan Island and another one just behind Camiguin Island. The drifters were released during the period from 1979 to 2003.

[4] This study deals with the vortex trains in the ocean. The vortex trains are observed in the Luzon Strait by the Argos satellite-tracked surface drifters and ENVISAT ASAR images acquired at the nearby Hong Kong Satellite Remote Sensing Ground Receiving Station. The significance of this study is not only to report the observed phenomenon, but also to develop methods for deriving of the dynamical parameters of OVT and mean flow. The next section gives a brief description of the geographic and hydrographic features of the study area. Section 3 contains satellite observations of the phenomenon and air-sea boundary conditions. Section 4 derives theoretical models of vortex radar image. On the basis of the models and radar backscatter section data taken from the ASAR images, the dynamical parameters of the vortex and vortex train are measured or calculated. Section 4 analyzes dynamical features of the OVT observed in the Luzon Strait. Sections 5 and Sections 6 give discussion and conclusions, respectively.

2. Study Area

2.1. Brief Geography

[5] The Luzon Strait, a study area of this paper, lies between Taiwan Island and Luzon Island as shown in Figure 1. The strait is approximately 386 km wide from south to north. The average depth is 1400 m [Guo *et al.*, 2004]. The strait connects the South China Sea (SCS) on the west and the Philippine Sea on the east. On the east side of the strait, there are two groups of islands: the Batan Islands in the north and Babuyan Islands in the south. These two groups of islands divide the strait into three smaller channels: the Bashi Channel is the northernmost one, which separates Taiwan from the Batan Islands, the Balintang Channel is in the middle, which separates the two islands, and the Babuyan Channel is the southernmost one, which separates Luzon Island from the Babuyan Islands.

[6] The Luzon Strait serves as a major channel for water exchange between the SCS and the Pacific. The Kuroshio flows along the east side of the Strait. Without topographic blockage, part of the Kuroshio water branches into the Strait forming the Kuroshio intrusion and the loop current [Centurioni *et al.*, 2004; Ho *et al.*, 2004]. Recent investigations reveal that the Luzon Strait is a source region for large amplitude ocean internal waves propagating westward into SCS [Liu *et al.*, 2004; Yuan *et al.*, 2006; Zheng *et al.*, 2007].

[7] The vortex trains to be studied in this paper were observed on the northwest side of Babuyan Island, the northernmost island of the Babuyan Islands. The Babuyan Claro Volcano is a major geological feature on the islands. The vent of volcano is 1180 m high above the sea level. The location of San Dionisio, the largest town on Babuyan Island, 19.5°N 121.9°E, may serve as reference coordinates for the islands.

2.2. Satellite-Tracked Drifter Trajectory Data

[8] During the period from 1979 to 2003, a great number of Argos satellite-tracked surface drifters were released in the Kuroshio and adjacent waters by the Tropical Ocean Global Atmosphere (TOGA) program, the World Ocean Circulation Experiment-Surface Velocity Program (WOCE-SVP), and Chinese oceanographic research programs. Figure 1 shows trajectories in and near the study area in November only. The drifter drogue was placed at a water depth of 15 m, so that the direct effects of atmospheric processes through sea surface winds on the drifter movement and current velocity calculation were ignorable [Niiler *et al.*, 1995]. The temporal resolution of drifter positioning for the data used in this study was one day [Hansen and Poulain, 1996].

[9] From Figure 1, one can see that there are six trajectories passing through the southern Luzon Strait. In particular, the two trajectories passing through Babuyan Islands show a train of three cyclonic vortices distributed from 20° to 20.5°N and from 120° to 121°E, and another one just behind Camiguin Island. The average distance between two centers of consecutive cyclonic vortices in the train is 50 km. The vortices occurred in the wake of Babuyan Islands, which serves as blunt obstacles in the ocean flow, and formed a vortex train in a line behind the islands. These striking features evidence their nature of OVT. The trajectories show that all the drifters moved northwestward ($\sim 315^\circ$ TN), implying that a northwestward ocean current flows from the Pacific into the SCS. The daily average current velocities derived from the trajectories are 1.3 ms^{-1} at the east border of the Strait (19° to 20.5°N, 121.5°E) and 0.6 ms^{-1} at the locations of vortex train (20° to 20.5°N, 120° to 121°E), respectively. The same features once again show up on the ENVISAT ASAR images of 19 November 2006 as shown in Figures 3a and Figures 3b and will be analyzed in details.

2.3. Estimated Parameters of the Vortex Train

[10] An enlarged map showing two Argos drifter trajectories with the vortex train signal is shown in Figure 2. The dynamical parameters of the vortices in the vortex train are measured for subsequent analysis. A period of drifter rotating around a vortex, T_d , can be determined directly from the trajectories. Thus the rotational angular velocity of

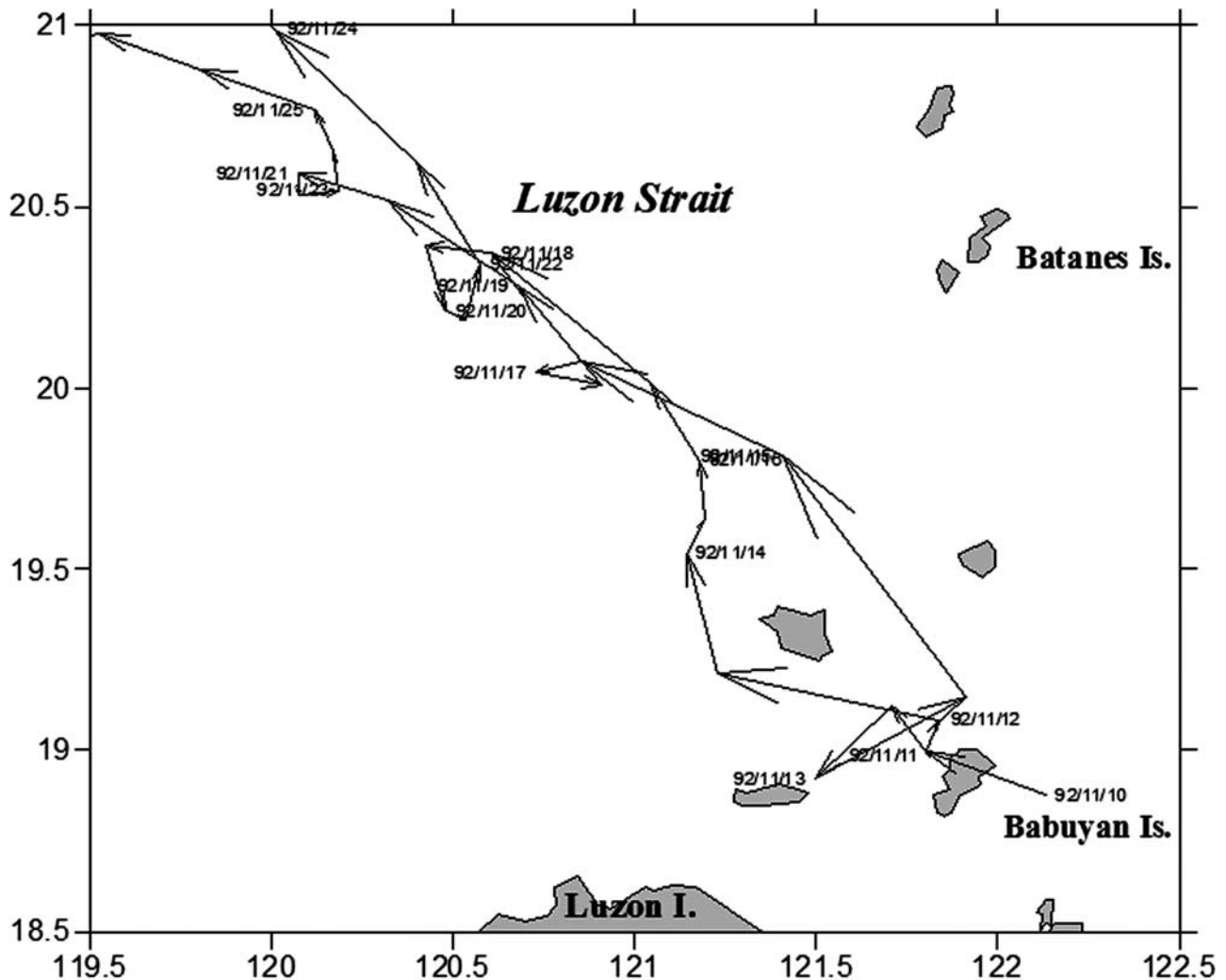


Figure 2. An enlarged map showing two Argos drifter trajectories with the vortex train signal. The dates marked on the trajectories are in YY/MM/DD.

the vortex, ω_d , can be estimated by $2\pi/T_d$. A vortex radius at which the drifter rotated, R , is determined by half of the maximum distance of vortex trajectory outedge. The radius determined by this method is an average distance of drifter to the vortex center, which does not necessarily coincide with the radius of the maximum rotational velocity. Then the drifter-determined daily mean tangent velocity can be estimated by $\omega_d R$. The results are listed in Table 1, in which the vortices are coded from number 1 in a northwestward order. One can see that the mean angular velocity of the vortices reaches $(2.66 \pm 0.56) \times 10^{-5} \text{ s}^{-1}$, 4–5 times faster than the Gulf Stream meso-scale eddies [Zheng *et al.*, 1984; Zheng and Yuan, 1989].

3. Satellite Observations and Air-Sea Boundary Conditions

3.1. ENVISAT ASAR Images

[11] The previous results have indicated that satellite SAR is a powerful sensor to record ocean processes. Its all weather and all time capacities break through restrictions of cloud cover and darkness, and its imaging resolution, up

to tens of meters, enables us to detect the fine structure of the ocean processes. In particular, SAR instruments are highly sensitive to the variation of spatial distribution of the sea surface roughness, which results from modulation effects of dynamical processes in the lower atmosphere and ocean [Fu and Holt, 1982; Meng, 2002; Zheng, 2005; Zheng *et al.*, 2001, 2004, 2006, 2007].

[12] The satellite SAR images used in this study are taken by ENVISAT, which was launched into a sun synchronous orbit by European Space Agency on 1 March 2002. Its orbit height is 786 km and inclination 98° . One of the most important payloads onboard ENVISAT is a C-band (5.331 GHz) SAR, which uses an active phased-array antenna with incidence angles between 15 and 45 degrees to provide dual polarization, and wide swath coverage imaging data. In Alternating Polarization Mode (AP Mode), the antenna provides three choices for different transmitting and receiving polarization combinations: VV and HH, or HH and HV, or VV and VH.

[13] The ASAR images used in this study were acquired and processed at the Hong Kong Satellite Remote Sensing

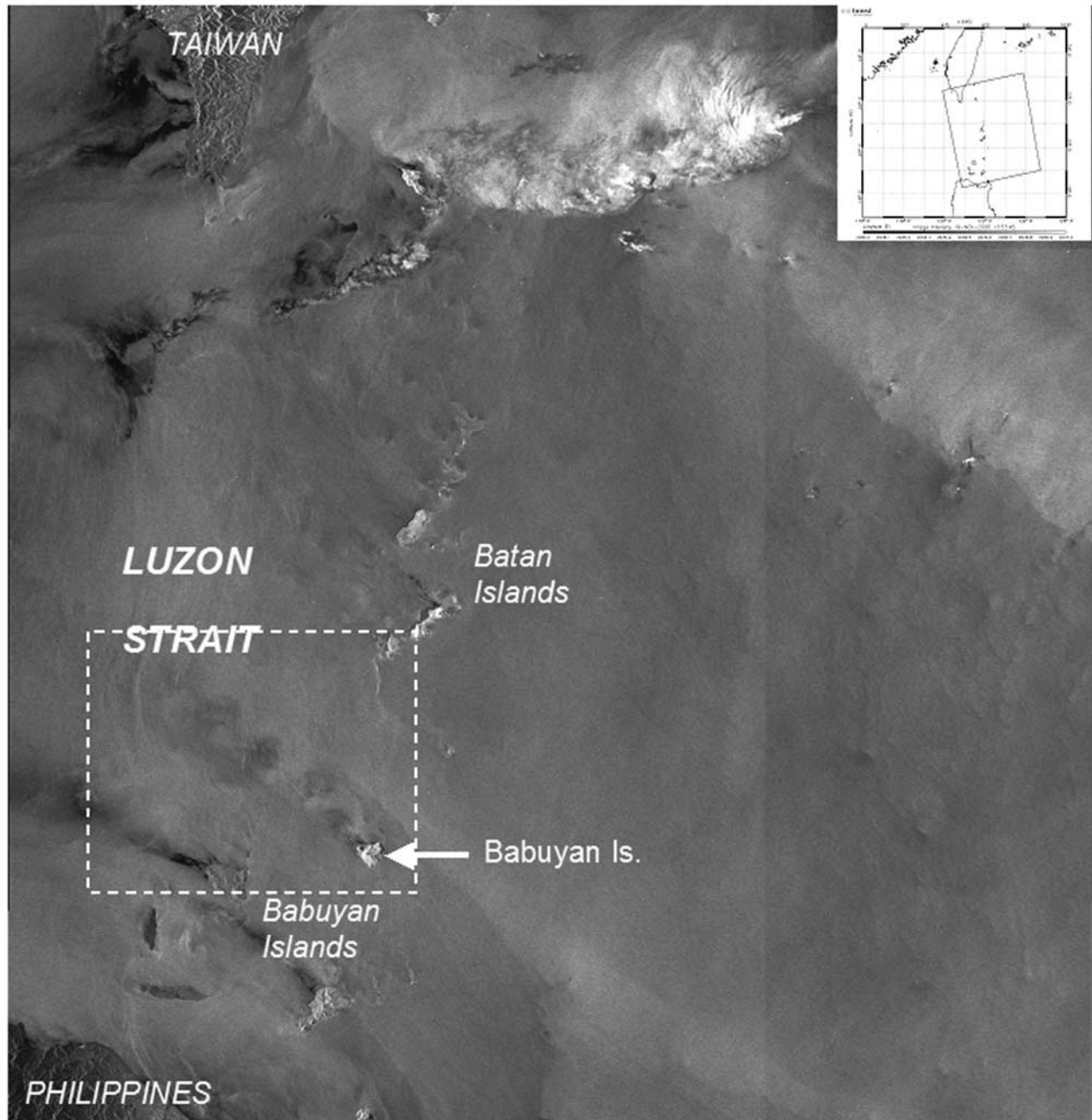


Figure 3a. A mosaic of ASAR images acquired at 13:53:45 UTC on 19 November 2006. The image coverage is shown in an inset on top right corner. A vortex train shows up in the dashed line box.

Ground Receiving Station, which was established at the Chinese University of Hong Kong in 2006. The images are generated by ASAR Image Mode. The nominal spatial resolution is 30 m, and the swath coverage is 100 km. The receivable area of antenna of the Hong Kong Station covers a circular region of 2500 km in radius centered at Hong Kong, enclosing most of the East Asia continent, Northwest Pacific from the Japan Sea to the Java Sea, and the Bay of Bengal in the North Indian Ocean.

[14] The study area is 600 to 800 km from Hong Kong Station. Thus high quality images, low noise, and low distortion may be ensured. Figure 3a shows a mosaic of

ASAR images acquired at 13:53:45 UTC on 19 November 2006. The image coverage is shown in the inset. On the mosaic image, one can see that the southern tip of Taiwan Island and the northern tip of Luzon Island are located at the top-left corner and lower-left corner, respectively. A bright area east of Taiwan on the central top of the image shows a rainfall area, which is beyond the scope of this study. The major portion of the image covers the Luzon Strait and the adjacent water of the Pacific. The landmarks of the Strait, the Batan Islands and the Babuyan Islands, are as marked in the image. The major feature of interest, as enclosed by a dashed line box in the image, is a vortex train distributed in

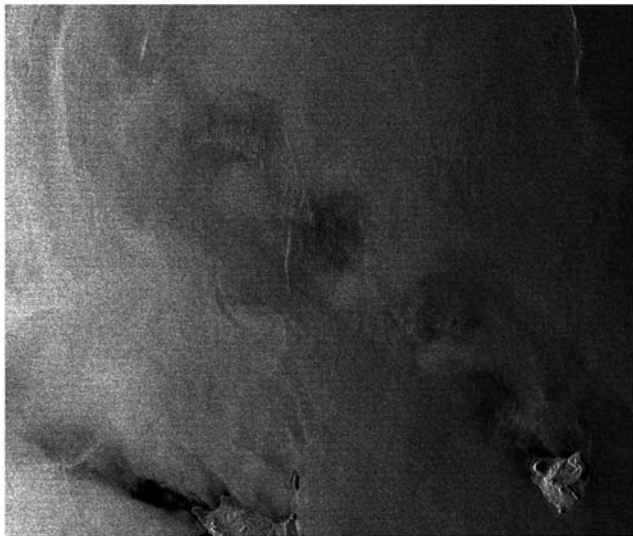


Figure 3b. Enlarged image of the vortex train taken from Figure 3a.

the northwest of Babuyan Island. An enlarged image of this sub-region is shown in Figure 3b. One can see that the vortex train imagery consists of five pairs of dark-bright, near-circular, vortex-like patterns, and the Babuyan Island looks like a train head.

3.2. Weather Conditions for ASAR Imaging

[15] The surface analysis weather charts before (12:00 UTC) and after (18:00 UTC) ASAR imaging are shown in Figures 4a and 4b. One can see that over adjacent East China, a weak high pressure (1024 mb) was moving eastward, meanwhile a cold front east of Taiwan was moving southeastward. While these two features had not yet influenced the study area at the imaging time. Over the study area were a clear sky and low wind conditions (wind speed $<5 \text{ ms}^{-1}$). Weather conditions observed at the nearest weather station, Itbayat Island located at $20^{\circ}47'N$ $121^{\circ}51'E$, 80 km north of the vortex train, are listed in Table 2.

[16] A MODIS (Moderate Resolution Imaging Spectroradiometer) thermal infrared composite image that was near-simultaneously taken with ASAR image (51 min later) is shown in Figure 5. One can see again the clear sky over the study area and no strong weather systems showing up.

[17] The weather maps and satellite images all show a clear and calm weather condition at the time of ASAR imaging. The sea surface wind speed obtained by linear interpolation was 2 ms^{-1} , implying a favorable condition for imaging of the sea surface process. Meanwhile, these boundary conditions further exclude the possibility of involvement of atmospheric processes in the vortex train images.

4. ASAR Image Interpretation

4.1. Recognition of OVT

[18] In section 2.2, the OVT in the Luzon Strait has been recognized from the Argos satellite-tracked drifter trajectories. In Figure 6, these trajectories are overlaid on the ASAR image. One can see that the cyclonic vortices on the trajectories are just distributed in the downstream side of vortex

train on the ASAR image. The two vortex train axes constitute a continuous straight line starting from the Babuyan Island. This evidences the common nature of two vortex trains, although they were not simultaneously observed.

[19] From the ASAR images shown in Figures 3a and 3b, the following conclusion is immediately derived. (1) The observation time was 13:53:45 UTC on 19 November 2006. (2) The OVT occurred within a range of 50 by 100 km from 19.5° to $20.0^{\circ}N$ and from 121.0° to $122.0^{\circ}E$ in the Luzon Strait. (3) The OVT consists of five pairs of cyclonic-anticyclonic vortices that are distributed in the wake of Babuyan Island. The axis of the OVT extends northwestward ($\sim 315^{\circ}$) starting from the Babuyan Island, implying existence of a northwestward mean flow-passing through the Luzon Strait. Later it will be verified that the center of the dark or bright area is the center of vortex, so that the average distance between the two centers of consecutive vortices and that between the two centers of adjacent cyclonic-anticyclonic vortices are measured as listed in Table 3.

4.2. Theoretical Models of Ocean Vortex Radar Image

[20] In order to extract dynamical parameters of the ocean vortex from the ASAR image, theoretical models of ocean vortex radar image must be derived from general radar imaging theories for ocean processes. In other words, the transformational relations between the radar imagery and vortex truth must first be set up.

[21] In general, an ocean surface radar image records a horizontal two-dimensional (Cartesian x - y) distribution of radar return signal intensity. The latter is parameterized by the backscatter cross section per unit area, which is defined as [Plant, 1990]

$$\sigma_{\circ}(\theta_0)_{ij} = 16\pi k_0^4 |g_{ij}(\theta_0)|^2 \psi(0, 2k_0 \sin \theta_0), \quad (1)$$

where θ_0 is the incidence angle, k_0 is the wave number of the radar waves, and Ψ is the two-dimensional wave number spectral density of the ocean surface wavefield which satisfies the Bragg resonant scatter condition, the incident radiation is in the x - z plane (z being the vertical direction), the indices ij denote the polarizations of the incident and backscattered radiation, respectively, and $g_{ij}(\theta_0)$ are the first-order scattering coefficients. For a given radar wave number and an incidence angle, the radar return signal intensity depends only on the two-dimensional wave number spectral density of the ocean surface wavefield, Ψ . The spatial variability of Ψ results in the intensity variability on radar images, so that generates imagery patterns or signatures of ocean processes.

Table 1. The Dynamical Parameters of Vortices Estimated From Drifter Trajectory Data

Vortex Time	yy/mm/dd	Period of Drifter, day	Angular Velocity, 10^{-5} s^{-1}	Radius km	Tangent Velocity Day, ms^{-1}
1	92/11/16–19	8.97	3.24	8.97	0.29
2	92/11/18–22	12.56	1.90	12.56	0.24
3	92/11/21–24	6.28	2.83	6.28	0.18
Mean			2.66 ± 0.56		0.24 ± 0.04

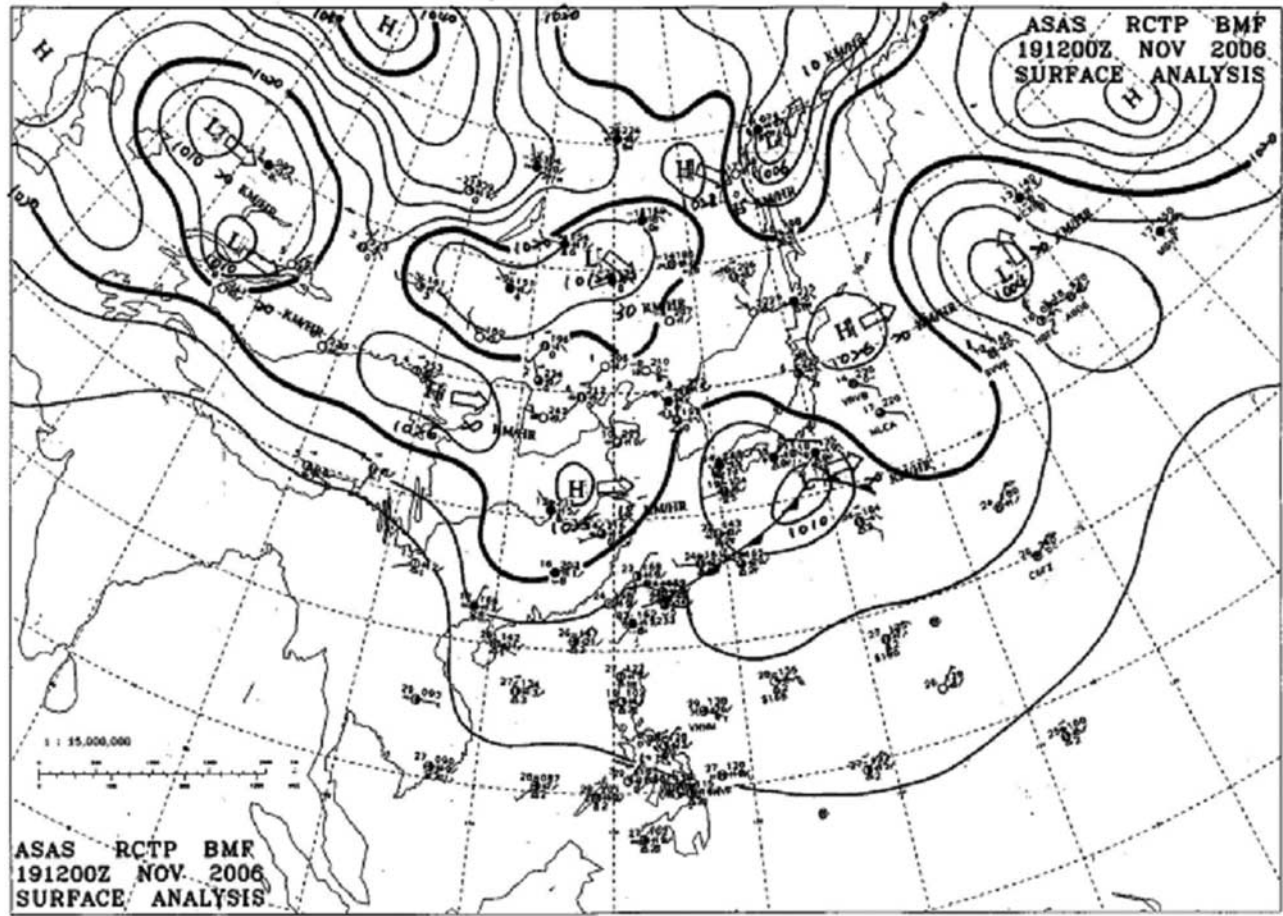


Figure 4a. Surface analysis weather charts of East Asia, 2-h before ASAR imaging (12:00 UTC, 19 November 2006).

[22] Considering the modulation of small ocean surface waves by wave-current interaction, Yuan [1997] derived the wave number spectral density of the high frequency ocean surface wavefield in the form of

$$\Psi = m_3^{-1} \left[m \left(\frac{u_*}{c} \right)^2 - 4\gamma k^2 \omega^{-1} - S_{\alpha\beta} \frac{\partial U_\beta}{\partial x_\alpha} \omega^{-1} \right] k^{-4} \quad (2)$$

for gravity-capillary wave band,

$$\Psi = m_4^{-1/2} \left[m \left(\frac{u_*}{c} \right)^2 - 4\gamma k^2 \omega^{-1} - S_{\alpha\beta} \frac{\partial U_\beta}{\partial x_\alpha} \omega^{-1} \right]^{1/2} k^{-4} \quad (3)$$

for capillary wave band,

where m , m_3 , and m_4 are coefficients (m_3 is called the spectral constant in this study later on), u_* is the friction velocity, c is the wave phase speed, γ is the viscosity of seawater, ω is the angular frequency of the ocean surface waves, k is the wave number of ocean surface waves, and

$$S_{\alpha\beta} \frac{\partial U_\beta}{\partial x_\alpha} = \left[\frac{\partial u}{\partial x} \cos^2 \phi + \left(\frac{\partial u}{\partial y} + \frac{\partial v}{\partial x} \right) \cos \phi \sin \phi + \frac{\partial v}{\partial y} \sin^2 \phi \right] / 2, \quad (4)$$

where u and v are current velocity components, and ϕ is the small wave direction.

[23] From equations (1)–(4), one can see that if the wind field and seawater viscosity are homogeneous, the current velocity field is a determining factor to generate the radar image of an ocean process. In our case, the ocean vortex and coordinate system are shown as a schema in Figure 7. The origin of the 2D horizontal coordinate system is chosen as the vortex center. The x axis is chosen as the ocean wave propagation direction, i.e., the sea surface wind direction. The y -direction is perpendicular to the x axis. Assume that the vortex is a cyclonic eddy with a counterclockwise rotating angle θ and a radial axis r .

[24] The rotational velocity structure of the vortex can be written as an empirical model [Zheng *et al.*, 1984]

$$V_\theta = \frac{\omega_E r^2}{r_0} \exp \left[\frac{1}{2} - \frac{1}{2} \left(\frac{r}{r_0} \right)^4 \right], \quad (5)$$

where ω_E is the rotational angular velocity, and r_0 is a radius at which the velocity takes a maximum value. Figure 8 shows a graph of (5). The data points are taken from the drifter trajectories shown in Figure 1 as listed in Table 1 and normalized by the maximum velocity. One can see that the empirical model fits the data quite well.

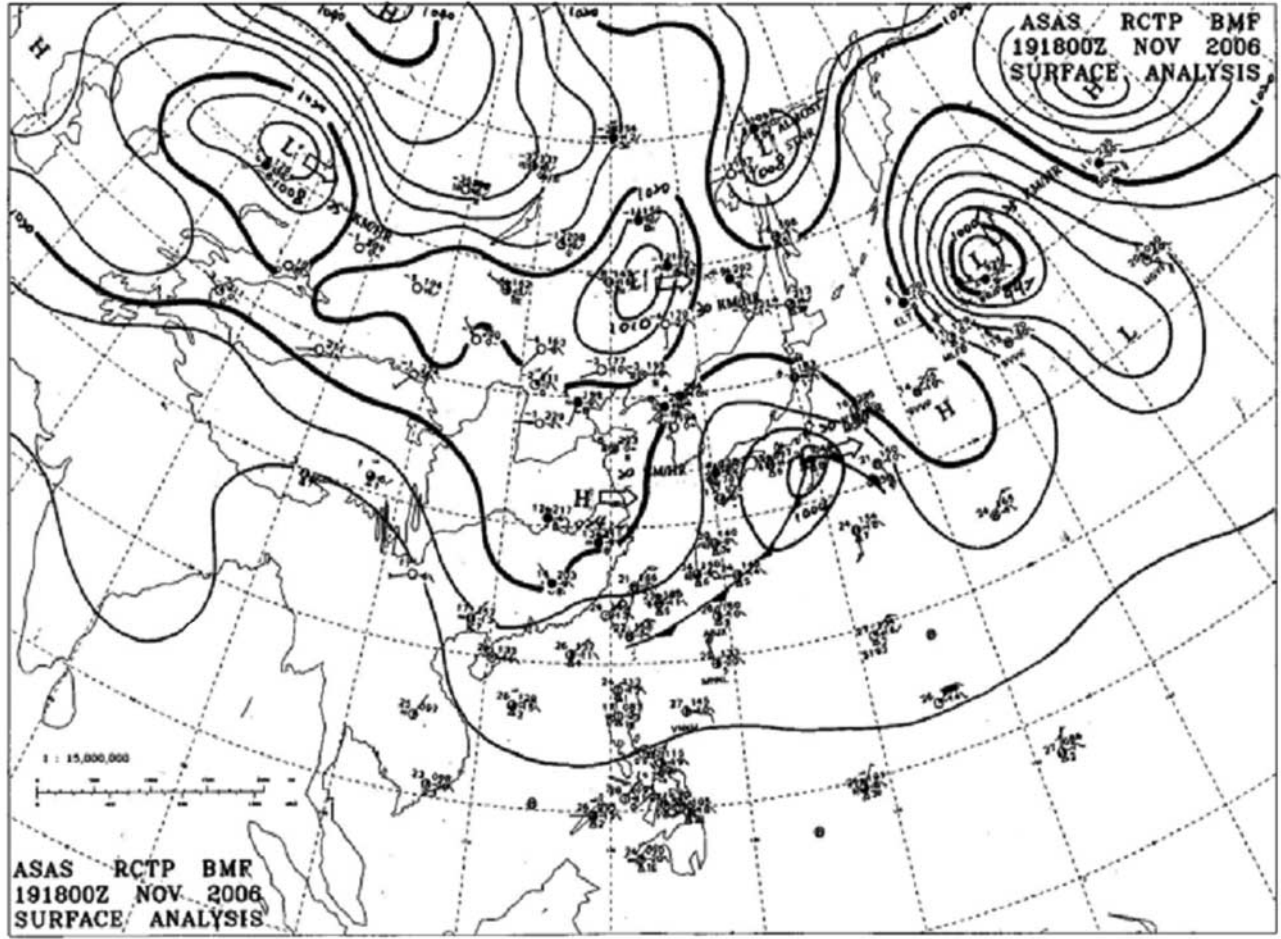


Figure 4b. Same as Figure 4a, but 4-h after ASAR imaging (18:00 UTC, 19 November 2006).

[25] On the other hand, the coordinate system setup implies that the small wave direction φ in equation (4) is zero. Thus (4) is simplified as

$$S_{\alpha\beta} \frac{\partial U_{\beta}}{\partial x_{\alpha}} = \left[\frac{\partial u}{\partial x} \right] / 2, \quad (6)$$

where $u = -V_{\theta} \sin\theta + V_r \cos\theta$, here $V_r \ll V_{\theta}$, so that the second term is negligible. Thus

$$\frac{\partial u}{\partial x} = \sin 2\theta \left[\frac{V_{\theta}}{r} - \frac{\partial V_{\theta}}{\partial r} \right]. \quad (7)$$

[26] Substituting (5) into (7) yields

$$\frac{\partial u}{\partial x} = \omega_E \sin 2\theta \left[2 \left(\frac{r}{r_0} \right)^5 - \frac{r}{r_0} \right] \exp \left[\frac{1}{2} - \frac{1}{2} \left(\frac{r}{r_0} \right)^4 \right] / 2. \quad (8)$$

[27] Assume that both wind field and seawater viscosity are homogeneous, Ψ in equation (2) can be written as

$$\Psi = \Psi_0 + \Psi_e, \quad (9)$$

where Ψ_0 represents a mean, homogeneous wavefield, and Ψ_e represents a variability of wavefield induced by an ocean vortex.

$$\Psi_e = m_3^{-1} \left[-S_{\alpha\beta} \frac{\partial U_{\beta}}{\partial x_{\alpha}} \omega^{-1} \right] k^{-4}. \quad (10)$$

[28] Substituting (6) and (8) into (10) yields

$$\Psi_e = m_3^{-1} k^{-4} \omega^{-1} \omega_E \sin 2\theta \left[\frac{r}{r_0} - 2 \left(\frac{r}{r_0} \right)^5 \right] \exp \left[\frac{1}{2} - \frac{1}{2} \left(\frac{r}{r_0} \right)^4 \right] / 4. \quad (11)$$

[29] Substituting (11) into (1) yields the variability of backscatter cross section per unit area

$$\sigma_{0e} = 4\pi k_0^4 \left| g_{ij}(\theta_0) \right|^2 m_3^{-1} k^{-4} \omega^{-1} \omega_E \cdot \sin 2\theta \left[\frac{r}{r_0} - 2 \left(\frac{r}{r_0} \right)^5 \right] \exp \left[\frac{1}{2} - \frac{1}{2} \left(\frac{r}{r_0} \right)^4 \right]. \quad (12)$$

Table 2. Weather Conditions Observed Within 2 h of ASAR Imaging at Itbayat Island

Time 19 Nov 2006	Air Temp., °C	Wind Speed, ms ⁻¹	Wind Direction	Cloud Coverage
12:00Z	26	5	SE	25%
15:00Z	28	1	SE	25%
13:54Z ^a	27 ^a	2 ^a	SE ^a	25% ^a

^aImaging time and interpolated values.

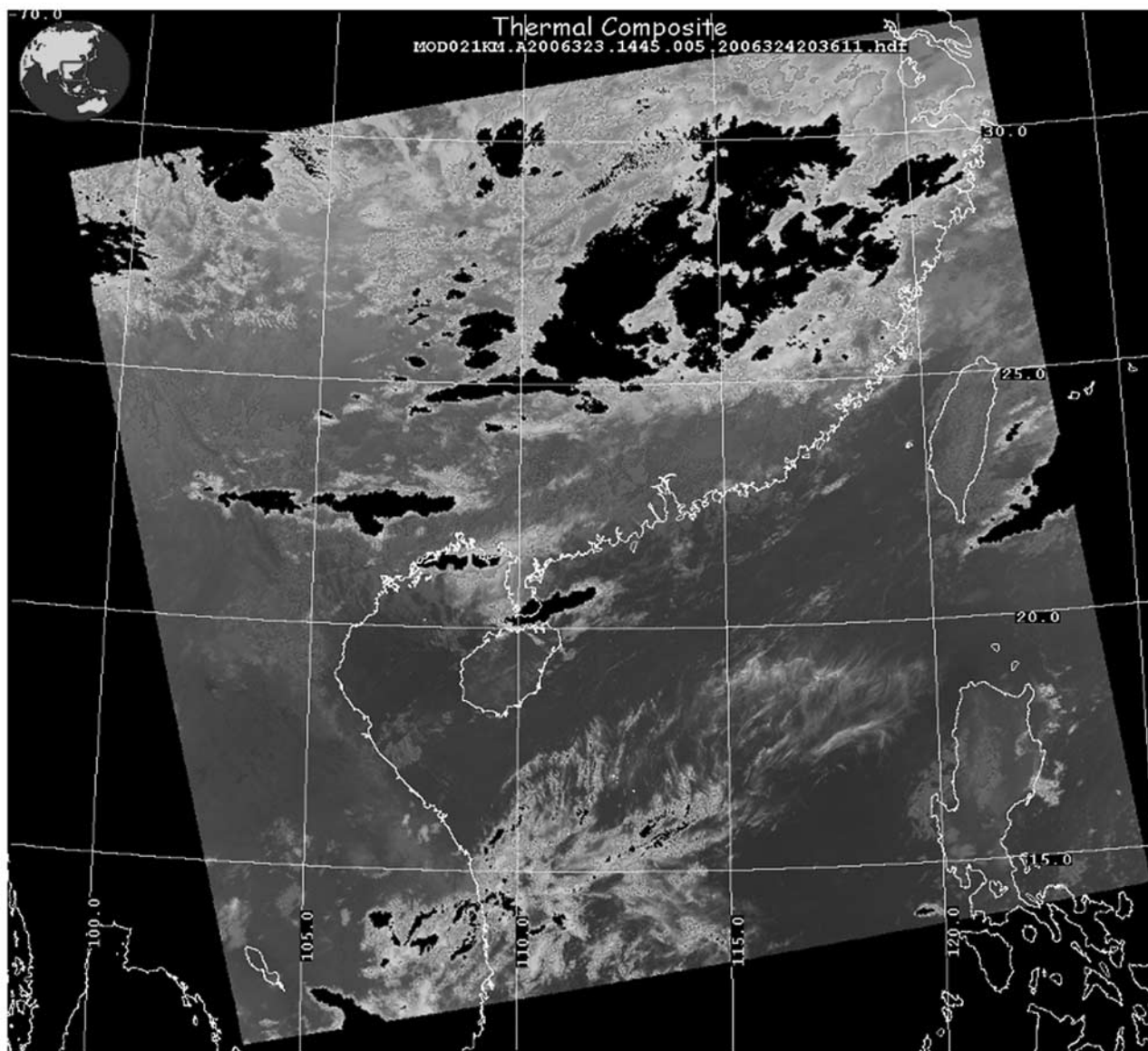


Figure 5. A MODIS thermal infrared composite image near synchronously taken with ASAR image (14:45 UTC, 19 November 2006).

[30] Equation (12) is the theoretical model of an ocean cyclonic vortex radar image being looked for. For the rotational angular velocity ω_E takes a negative value, model (12) represents an anti-cyclonic vortex.

[31] Figure 9 shows a comparison of the theoretical model with a σ_{0e} profile taken from a transect across the third cyclonic vortex behind Babuyan Island in Figures 3a and 3b. One can see that as a first order approximation, the model fits a general trend in radar imagery, in particular, the increasing edge. Obviously, the imagery also contains other high frequency signals or noises, which make the imagery deviate from the vortex model.

4.3. Inferences of Theoretical Models

[32] From the theoretical model of ocean vortex radar image, equation (12), the following inferences can directly be derived.

4.3.1. The Center of True Vortex

[33] Equation (12) indicates that the radar backscatter cross section σ_{0e} increases with r , for $r < r_0$. Let $r = 0$, (12) gives $\sigma_{0e} = 0$. This means that the geometric center of the vortex imagery is the center of the true vortex. Thus the distances between two consecutive vortices and two rows of vortices can be measured from the ASAR image. These data are important parameters for dynamical analysis of OVT (see section 5). The measured results are listed in Table 3.

4.3.2. The Maximum Rotational Velocity Radius

[34] Equations (5) and (12) show that the maximum rotational velocity radius, r_0 , is a key parameter in determining the velocity structure of vortex. However, this parameter cannot directly be measured from the vortex radar image. A related parameter, which can be measured

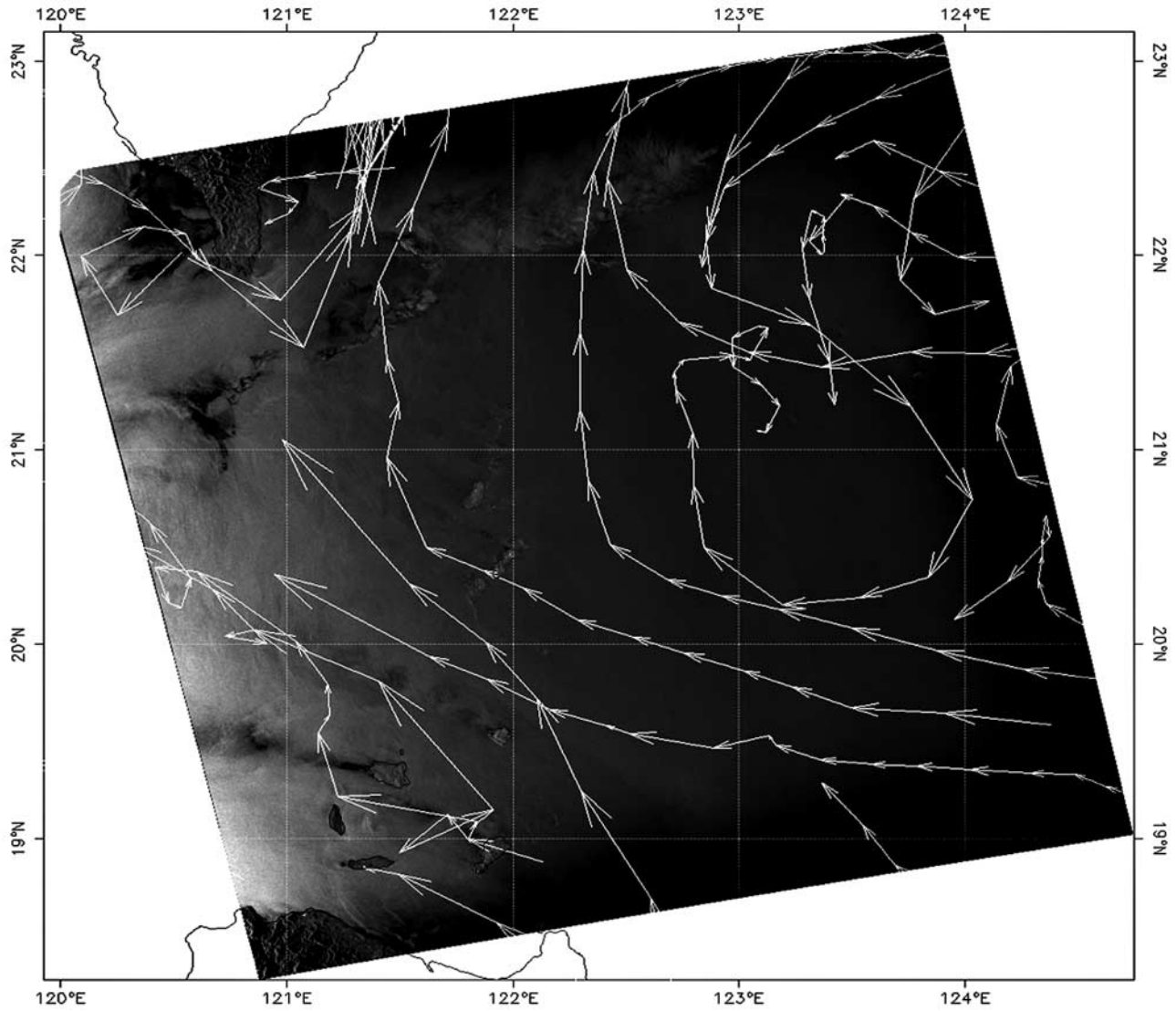


Figure 6. A composite image of ASAR image with Argos satellite-tracked drifter trajectories of November.

from radar image, is a maximum radar backscatter radius defined as r_m . According to the definition, r_m satisfies

$$\left. \frac{\partial \sigma_{0e}}{\partial r} \right|_{r=r_m} = 0. \tag{13}$$

[35] Solving equation (13) results to the physically sound solutions

$$r_{m1} = 0.542r_0, \text{ with } \left. \frac{\partial^2 \sigma_{0e}}{\partial r^2} \right|_{r=r_{m1}} > 0, \tag{14a}$$

Table 3. Distances Between Two Consecutive Vortices and Two Rows of Vortices Measured From the ASAR Image

Vortex Pair	Distance of Two Vortices (a) km		Distance of Two Vortex Row (h) km
	Cyclonic	Anti-Cyclonic	
2			6.30
3	22.92	18.91	8.60
4	22.92	25.21	8.02
5	22.92	22.92	9.74
Mean	22.6 ± 1.9		8.2 ± 1.2

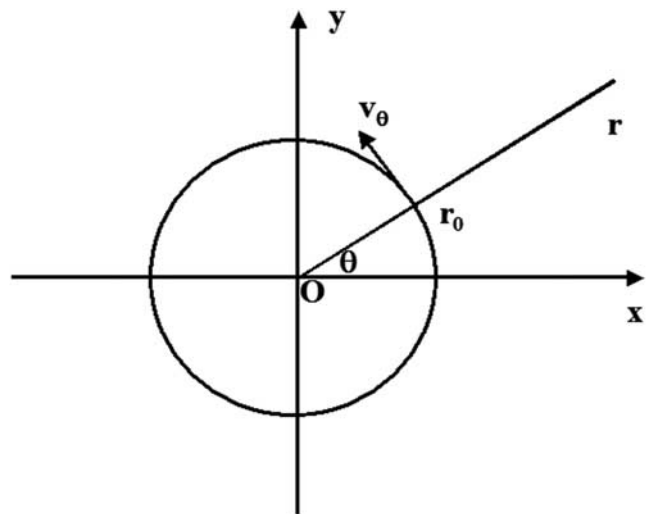


Figure 7. A schema of the cyclonic vortex and the coordinate system.

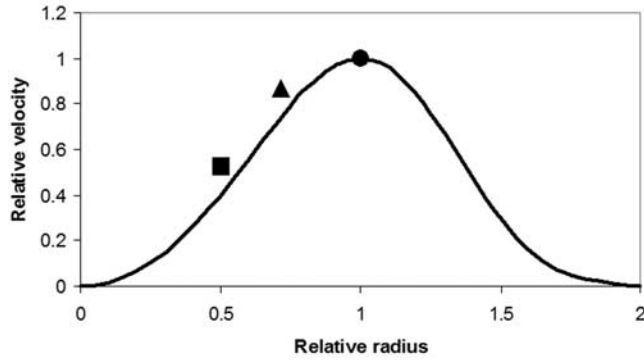


Figure 8. An empirical model of ocean vortex tangent velocity distribution. The data points are taken from the Argos satellite-tracked drifter trajectories shown in Figure 1 and normalized by the maximum velocity.

and

$$r_{m2} = 1.307r_0, \text{ with } \left. \frac{\partial^2 \sigma_{0e}}{\partial r^2} \right|_{r=r_{m2}} < 0. \quad (14b)$$

[36] Comparing with the theoretical curve in Figure 9, one can see that these two solutions correspond to the minimum value at pixel 34 and the maximum at pixel 82, respectively. Thus after r_m is measured from the radar image, the maximum rotational velocity vortex radius, r_0 , can be calculated by (14a) or (14b). In the case shown in Figure 9, the maximum rotational velocity radius r_0 is determined to be 4.70 km.

4.3.3. The Vortex Rotational Angular Velocity and Spectral Constant m_3

[37] If the radar backscatter cross section σ_{0e} at a given r is obtained from an ocean vortex imagery, the rotational angular velocity ω_E and spectral constant m_3 can be calculated by (12), if one of them is known. Taking the

case of Figure 9 as an example, from radar imagery transect data we obtain the radar backscatter cross section at vortex center $\sigma_{0e}(0) = 0.0149$, which serves as a background backscatter cross section, and the maximum radar backscatter section at $r = 6.15$ km $\sigma_{0e}(6.15 \text{ km}) = 0.0276$. Thus vortex-induced increment in radar backscatter cross section at $r = 6.15$ km $\Delta\sigma_{0e}(6.15 \text{ km})$ should be 0.0127. Other parameters are as follows: $\lambda_0 = 5.7$ cm; $\theta_0 = 30^\circ$; $|g_{ij}(\theta_0)|^2 = 0.929$ (salinity 35 psu, water temperature 22°C , HH polarization); $\omega = 35.26 \text{ s}^{-1}$; $\theta = -45^\circ$; $r_o = 4.70$ km, and

$$\left[\frac{r}{r_0} - 2 \left(\frac{r}{r_0} \right)^5 \right] \exp \left[\frac{1}{2} - \frac{1}{2} \left(\frac{r}{r_0} \right)^4 \right] \Bigg|_{r=6.15 \text{ km}} = -2.42.$$

Substituting these parameters into (12) yields

$$\omega_E m_3^{-1} = 1.54 \times 10^{-2}. \quad (15)$$

[38] On the other hand, the data listed in Table 1 indicate that a reasonable estimate of the vortex angular velocities should be $\omega_E = 3 \times 10^{-5} \text{ s}^{-1}$. Thus from (15) we obtain an estimate of spectral constant m_3 as 1.95×10^{-3} .

4.4. Dynamical Analysis of OVT

[39] A physical model of OVT is schematically shown in Figure 10. The parameters are defined as follows: U_0 , the current velocity of mean or undisturbed flow; U_e , the propagation velocity of vortex; a , the distance between two consecutive vortices; and h , the distance between two rows of vortices.

[40] Based on this model, the vortex propagation problem can be solved by solving the following two equations. The first equation describes the relation between U_0 and U_e [Chopra and Hubert, 1964]

$$U_0 - U_e = \frac{K}{2a} \tanh \left(\frac{\pi h}{a} \right) \quad (16)$$

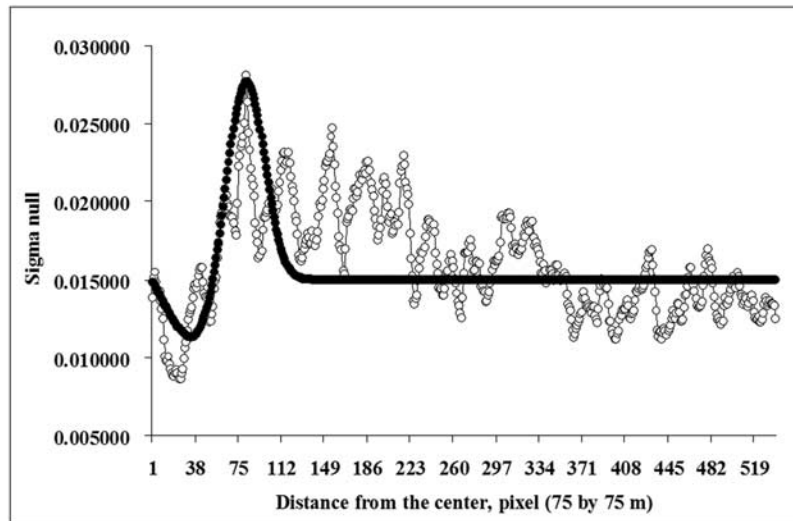


Figure 9. A comparison of the theoretical model (12) (solid curve) with a σ_{0e} profile (data points) taken from a transect across the third cyclonic vortex behind Babuyan Island in Figures 3a and 3b. Pixel size is 75 by 75 m.

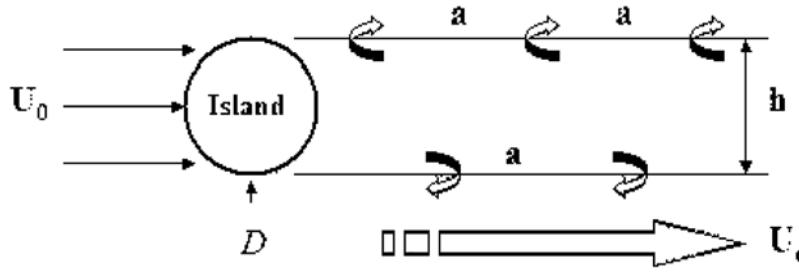


Figure 10. A schema of physical model of ocean vortex train.

where K is defined as the vortex circulation strength

$$k = 2\pi r_0 V_\theta. \quad (17)$$

[41] The second equation is derived by *Tsuchiya* [1969]

$$(2B - A)\chi^2 + (2A - 3B)\chi + (B - A + B/4A) = 0, \quad (18)$$

where $\chi = U_e/U_0$, $A = \coth(\pi h/a)$ and $B = \pi h/a$. In the case of interest, $h/a = 0.363$, so that $A = 1.229$, and $B = 1.139$. Substituting these parameters into (19) and taking a larger solution yields [*Li et al.*, 2000]

$$\chi = U_e/U_0 = 0.885. \quad (19)$$

[42] The reasonable estimate of angular velocity should be $3 \times 10^{-5} \text{ s}^{-1}$. The maximum velocity radius has been determined as $r_0 = 4.70 \text{ km}$. Substituting these parameters into (18) yields the vortex circulation strength $K = 4161 \text{ m}^2\text{s}^{-1}$. Substituting the K value into (17) yields

$$U_0 - U_e = 0.0749 \text{ ms}^{-1}. \quad (20)$$

[43] Solving (19) and (20) yields $U_0 = 0.65 \text{ ms}^{-1}$ and $U_e = 0.58 \text{ ms}^{-1}$. On the other hand, the drifter trajectories in November shown in Figure 1 give an average mean flow velocity $(0.70 \pm 0.25) \text{ ms}^{-1}$, which is coincided with the above estimates. Meanwhile, an estimate of the vortex shedding rate $F (= U_e/a)$ is derived as $2.57 \times 10^{-5} \text{ s}^{-1}$.

[44] The Reynolds number is defined as [*Kundu*, 1990]

$$R_e = \frac{UD}{A_H}, \quad (21)$$

where $U [= O(50 \text{ cms}^{-1})]$ and $D [= O(1 \times 10^6 \text{ cm})]$ are the characteristic velocity of mean flow and length scale of island diameter, respectively, and A_H is the horizontal turbulent viscosity. Thus in the case of interest a reasonable estimate of the Reynolds number is $R_e = O(50 \text{ to } 500)$, if A_H is generally chosen as $1 \times 10^5 \text{ cm}^2\text{s}^{-1}$ to $1 \times 10^6 \text{ cm}^2\text{s}^{-1}$ for the mesoscale or sub-mesoscale ocean processes [*Zheng and Yuan*, 1989].

[45] The Rossby number defined as

$$\varepsilon = \frac{U}{fL}, \quad (22)$$

where $f (= 2\Omega \sin\Theta)$ is the local Coriolis parameter and L is the length scale of phenomenon, is used to estimate the

dynamical scale of a geophysical fluid phenomenon. From the Argos satellite-tracked drifter trajectory data, the mean angular velocity of vortices is determined as $(2.66 \pm 0.56) \times 10^{-5} \text{ s}^{-1}$. In the above section, the vortex shedding rate is estimated as $2.57 \times 10^{-5} \text{ s}^{-1}$ from ASAR images. While the local Coriolis parameter $f(\Theta = 20^\circ)$ is $4.97 \times 10^{-5} \text{ s}^{-1}$. Thus for an individual vortex, the Rossby number ε is $O(0.4)$, and for the KVS, it is $O(0.5)$. This implies that vortex train observed in the study area has a dynamically sub-mesoscale nature, i.e., the length scale is $O(50 \text{ km})$, and the Rossby number is within a range of $0.1 < \varepsilon < 1$.

5. Discussion

[46] There are similarities between the atmospheric KVS and oceanic vortex train. However, their spatial scales are distinct. For example, the distance between two consecutive atmospheric vortices usually is $O(100 \text{ km})$ [*Tsuchiya*, 1969; *Thomson et al.*, 1977; *Turner and Warren*, 1988], five times larger than that in the case of interest. The vortex life spans, estimated by the length of KVS divided by the vortex propagation velocity, are also distinct. In the atmosphere, it is on the order of a couple of hours [*Li et al.*, 2000], while in the studied ocean case it may last much longer, e.g., longer than five days. On the satellite images, they have distinct imagery signatures. The atmospheric KVS are usually visualized by zigzag low-level cloud patterns, but not for the OVT.

[47] Satellite-tracked drifter trajectories and OVT signatures on ASAR images used in this study reveal that a strong current flows directly from the Pacific (Philippine Sea) to SCS passing through the south Luzon Strait in November. The average surface current velocity is around 0.7 ms^{-1} , and the direction is around 315° TN . Using the methods developed in this study, the angular velocity of ocean vortex can be calculated by the radar backscatter cross section profile taken along a vortex radial transect, if the spectral constant m_3 is independently determined. Then, the mean flow velocity can be calculated using the OVT dynamical models.

6. Conclusions

[48] The Argos satellite-tracked surface drifter trajectory data and ENVISAT ASAR images are used to observe the OVTs in the Luzon Strait. Two cases of vortex trains that occurred in November, local fall, are observed in the wake of Babuyan Island. The first train of three cyclonic vortices showing up on drifter trajectories is distributed in the northwest of Babuyan Islands from 20° to 20.5°N and from

120° to 121°E. The second train consisting of two parallel rows, five pairs of alternating cyclonic-anticyclonic vortices were observed on the ASAR images of 19 November 2006. The second train occurred on the upstream side of the first one from 19.5° to 20.0°N and from 121.0° to 122.0°E. The total length of the vortex train along the axis reaches about 250 km. All vortices propagate northwestward ($\sim 315^\circ$ TN). The mean angular velocity is $(2.07 \pm 0.18) \times 10^{-5} \text{ s}^{-1}$.

[49] Theoretical models of the ocean vortex radar image are derived from general radar imaging theories for ocean processes. These functional relations are used to extract dynamical parameters of the ocean vortex and the vortex train from ASAR imagery signatures. The results are as follows: The distances between two consecutive vortices and two rows of vortices are $(22.6 \pm 1.9) \text{ km}$ and $(8.2 \pm 1.2) \text{ km}$, respectively. The maximum rotational velocity radius is determined to be 4.70 km. The vortex rotational angular velocity ω_E is $O(3 \times 10^{-5} \text{ s}^{-1})$, if the spectral constant m_3 is taken as 1.95×10^{-3} .

[50] Dynamical analyses give reasonable estimates of OVT dynamical parameters. The current velocity of mean or undisturbed flow as $U_0 = 0.65 \text{ ms}^{-1}$, which coincides with the average mean flow velocity $(0.70 \pm 0.25) \text{ ms}^{-1}$ measured by drifters, and the propagation velocity of vortex $U_e = 0.58 \text{ ms}^{-1}$. The estimated vortex shedding rate $F (= U_e/a)$ is $2.57 \times 10^{-5} \text{ s}^{-1}$. The Reynolds number is $R_e = O(50 \text{ to } 500)$, if A_H is chosen as $1 \times 10^5 \text{ cm}^2 \text{ s}^{-1}$ to $1 \times 10^6 \text{ cm}^2 \text{ s}^{-1}$. For an individual vortex, the length scale is $O(5 \text{ km})$, and the Rossby number is $O(0.4)$. For the OVT, the length scale is $O(20\text{--}50 \text{ km})$, and the Rossby number is $O(0.5)$, implying that vortex trains observed in the Luzon Strait are of sub-mesoscale in nature.

[51] **Acknowledgments.** The authors thank the Hong Kong Satellite Remote Sensing Ground Receiving Station for providing ENVISAT ASAR data and to Shih-Jen Huang of National Taiwan Ocean University for providing the surface weather data. This work was supported by the Chinese University of Hong Kong, the National Natural Science Foundations of China (40406009 for Hu), and partly by ONR through grants N00014-05-1-0605 (for Li), N00014-05-1-0328, N00014-05-1-0606, and NASA JPL through subcontract NMO710968 (for Zheng).

References

- Centurioni, L. R., P. P. Niiler, and D. K. Lee (2004), Observations of inflow of Philippine Sea surface water into the South China Sea through the Luzon Strait, *J. Phys. Oceanogr.*, *34*, 113–121.
- Chopra, K. P., and L. F. Hubert (1964), Kármán vortex streets in earth's atmosphere, *Nature*, *203*, 1341–1343.
- Fu, L.-L., and B. Holt (1982), *Seasat Views Oceans and Sea Ice With Synthetic Aperture Radar*, National Aeronautics and Space Administration, Jet Propulsion Laboratory, JPL Publication 81–120, Pasadena, CA.
- Guo, B., Z. Huang, P. Li, W. Ji, G. Liu, and J. Xu (2004), *Marine Environment of Offshore and Adjacent Ocean Areas of China*, pp. 189–223, Ocean Press, Beijing.
- Hansen, D. V., and P. M. Poulain (1996), Quality control and interpolation of WOCE/TOGA drifter data, *J. Atmos. Ocean Technol.*, *13*, 900–909.
- Ho, C.-R., Q. Zheng, N.-J. Kuo, C.-H. Tsai, and N. E. Huang (2004), Observation of the Kuroshio intrusion region in the South China Sea from AVHRR data, *Int. J. Remote Sens.*, *25*, 4583–4591.
- Kundu, P. K. (1990), *Fluid Dynamics*, pp. 321–338, Academic Press, San Diego.
- Li, X., P. Clemente-Colón, W. G. Pichel, and P. W. Wachon (2000), Atmospheric vortex streets on a RADARSAT SAR image, *Geophys. Res. Lett.*, *27*, 1655–1658.
- Liu, A. K., S. R. Ramp, Y. Zhao, and T. Y. Tang (2004), A case study of internal solitary wave propagation during ASIAEX 2001, *IEEE J. Ocean Eng.*, *29*, 1144–1156.
- Meng, J. (2002), *A Study of Information Extraction Technology of Ocean Internal Waves From SAR Images*, Ph.D. Dissertation, pp. 1–114, Ocean University of Qingdao, Qingdao, China.
- Niiler, P. P., A. S. Sybrandt, K. Bi, P. M. Poulain, and D. Bitterman (1995), Measurements of the water-following capability of holey-sock and TRISTAR drifters, *Deep Sea Res.*, *42*, 1951–1964.
- Plant, W. J. (1990), Bragg scattering of electromagnetic waves from the air/sea interface, in *Surface Waves and Fluxes, vol. II- Remote Sensing*, edited by G. L. Geernaert and W. J. Plant, pp. 41–108, Kluwer Academic Publishers, London.
- Taneda, S. (1965), Experimental investigation of vortex street, *J. Phys. Soc. Jpn.*, *20*, 1714–1721.
- Thomson, R. E., J. F. R. Gower, and N. W. Bowker (1977), Vortex street in the wake of the Aleutian Islands, *Mon. Weather Rev.*, *105*, 873–884.
- Tsuchiya, K. (1969), The clouds with the shape of Kármán vortex street in the wake of Cheju Island, *Korea J. Meteorol. Soc. Jpn.*, *47*, 457–464.
- Turner, J., and D. E. Warren (1988), A multi-spectral satellite image of a vortex street in the lee of Jan Mayen, *Weather*, *43*, 363–369.
- Von Kármán, T. (1954), *Aerodynamics*, pp. 1–203, McGraw-Hill, New York.
- Yuan, Y. (1997), Representation of high frequency spectra of ocean waves and the basis for analyzing SAR images, *Chin. J. Oceanol.*, *28*, suppl., 1–5.
- Yuan, Y., Q. Zheng, D. Dai, X. Hu, F. Qiao, and J. Meng (2006), The mechanism of internal waves in the Luzon Strait, *J. Geophys. Res.*, *111*, C11S17, doi:10.1029/2005JC003198.
- Zheng, Q. (2005), Comments on “Can near-inertial internal waves in the East Sea be observed by synthetic aperture radar?”, *Geophys. Res. Lett.*, *32*, L20606, doi:10.1029/2005GL023770.
- Zheng, Q., and Y. Yuan (1989), A study on analytical model of decay of mesoscale eddies on the continental shelf, *Sci. China Ser. B*, *32*, 1135–1143.
- Zheng, Q., V. Klemas, and N. E. Huang (1984), Dynamics of the slope water off New England and its influence on the Gulf Stream as inferred from satellite IR data, *Remote Sens. Environ.*, *15*, 135–153.
- Zheng, Q., Y. Yuan, V. Klemas, and X.-H. Yan (2001), Theoretical expression for an ocean internal soliton SAR image and determination of the soliton characteristic half width, *J. Geophys. Res.*, *106*(C12), 31,415–31,423.
- Zheng, Q., P. Clemente-Colón, X.-H. Yan, W. Timothy Liu, and N. E. Huang (2004), Satellite SAR detection of Delaware Bay plumes: Jet-like feature analysis, *J. Geophys. Res.*, *109*, C03031, doi:10.1029/2003JC002100.
- Zheng, Q., L. Li, X. Guo, Y. Ge, D. Zhu, and C. Li (2006), SAR Imaging and hydrodynamic analysis of ocean bottom topographic waves, *J. Geophys. Res.*, *111*, C09028, doi:10.1029/2006JC003586.
- Zheng, Q., R. D. Susanto, C.-R. Ho, Y. T. Song, and Q. Xu (2007), Statistical and dynamical analyses of generation mechanisms of solitary internal waves in the northern South China Sea, *J. Geophys. Res.*, *112*, C03021, doi:10.1029/2006JC003551.
- X. Hu, The Key Laboratory of Marine Science and Numerical Modeling, The First Institute of Oceanography, State Oceanic Administration, 6 Xianxialing Road, Laoshan District, Qingdao, Shandong, 266061 China.
- C. Li, 208 C Howe-Russell Geoscience Complex Coastal Studies Institute, Department of Oceanography and Coastal Sciences, Louisiana State University, Baton Rouge, LA, 70803, USA.
- H. Lin, J. Meng, and Y. Zhang, Room 615 Esther Lee Building, Chung Chi College, Institute of Space and Earth Information Sciences, The Chinese University of Hong Kong, Shatin, Hong Kong.
- Y. T. Song, Jet Propulsion Laboratory, California Institute of Technology, M/S 300-323, 4800 Oak Grove Dr., Pasadena, CA, 91109, USA.
- Q. Zheng, Department of Atmospheric and Oceanic Science, University of Maryland, 2423 Computer Space Science Building, College Park, MD 20742-2425, USA. (quanan@atmos.umd.edu)